ACS APPLIED MATERIALS & INTERFACES

Research Article

www.acsami.org

Morphologically Robust $NiFe_2O_4$ Nanofibers as High Capacity Li-Ion Battery Anode Material

Christie Thomas Cherian,[†,‡] Jayaraman Sundaramurthy,[¶,§,‡] M. V. Reddy,[†] Palanisamy Suresh Kumar,[§] Kalaivani Mani,[§] Damian Pliszka,[§] Chorng Haur Sow,[†] Seeram Ramakrishna,*[,¶,§] and B. V. R. Chowdari*[,†]

[†]Department of Physics, National University of Singapore, 2 Science Drive 3, Singapore 117551

[¶]NUS Nanoscience and Nanotechnology Initiative, National University of Singapore, 2 Engineering Drive 3, Singapore 117576

[§]Department of Mechanical Engineering, National University of Singapore, 2 Engineering Drive 3, Singapore 117576

Supporting Information

ABSTRACT: In this work, the electrochemical performance of $NiFe_2O_4$ nanofibers synthesized by an electrospinning approach have been discussed in detail. Lithium storage properties of nanofibers are evaluated and compared with $NiFe_2O_4$ nanoparticles by galvanostatic cycling and cyclic voltammetry studies, both in half-cell configurations. Nanofibers exhibit a higher charge-storage capacity of 1000 mAh g^{-1} even after 100 cycles with high Coulmbic efficiency of 100 % between 10 and 100 cycles. Ex situ microscopy studies confirmed that cycled nanofiber electrodes maintained the morphology and remained intact even after 100 charge–discharge cycles. The $NiFe_2O_4$ nanofiber electrode does not experience any structural stress and eventual pulverisation during lithium cycling and hence provides an efficient electron conducting pathway. The excellent electrochemical performance of $NiFe_2O_4$ nanofibers is due to the unique porous morphology of continuous nanofibers.

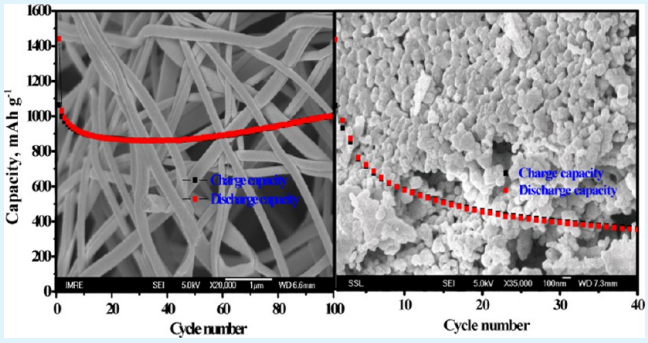

KEYWORDS: *$NiFe_2O_4$, nanofibers, electrospinning, anode, Li-ion battery, impedance*

INTRODUCTION

Light weight rechargeable batteries with higher energy density are in greater demand as an energy source for various portable electronic devices like digital cameras, cell phones, and laptops.[1] Growing environmental concerns around the globe are driving the development of advanced batteries for off-grid energy storage and electric vehicles (EVs).[2] Among them, lithium-ion batteries (LIBs) have been considered as future energy storage for hybrid EVs, plug-in hybrid EVs, and EVs, which require relatively light weight with high power and energy densities.[3] High-energy density batteries can be achieved by employing electrodes with higher specific capacities than the commercially available electrodes such as graphite having a theoretical specific capacity of 372 mAh g^{-1}. Interestingly, transition metal oxides can undergo a "conversion" reaction with lithium and deliver high capacity by utilizing all possible oxidation states of transition metals.[4]

Iron-based spinel oxides like Fe_3O_4[5] and ferrites with general formula AFe_2O_4 (A= Ni, Co, Zn, Cu, Mg, Cd)[6−11] have been explored for their Li-cyclability. Chen et al. studied the Li-insertion reactions of several cubic iron spinels at room temperature, MFe_2O_4 with M^{2+} = Mn, Fe, Co, Ni, Cu, Zn, and Cd by using butyl-Li, and concluded that ferrites with inverse spinel structure can be incorporated with more Li ions, compared to mixed and normal spinel.[12] Among various ferrites, $NiFe_2O_4$ has an inverse spinel structure with Ni^{2+} and half of the Fe^{3+} cation occupying the octahedral site and the remaining Fe^{3+} on the tetrahedral site, $Fe^{3+}[Ni^{2+}, Fe^{3+}]O_4$. Moreover, it can electrochemically react with 8 mols of Li delivering a capacity of 915 mAh g^{-1}.[7] Importantly, both nickel and iron are abundant elements on earth and relatively nontoxic.[14] With these advantages, $NiFe_2O_4$ can be explored as a prospective anode material for high energy LIBs apart from the drawback of marked hysteresis in voltage between charge and discharge.

In earlier reports, it has been reported that $NiFe_2O_4$ exhibit drastic capacity fading irrespective of synthesis approach and processing conditions.[7,15] Thus, several efforts have been adopted to enhance the long-term Li-cycling of $NiFe_2O_4$ nanostructures by adopting different synthesis approaches for partial substitutions of host-structures with metal-cations, controlling the morphology and particle sizes.[13,16,17] Tirado et al. carried out Li-cycling properties of $NiFe_2O_4$ and investigated the origin of capacity fading upon cycling.[7]

Received: May 20, 2013
Accepted: September 20, 2013
Published: September 20, 2013

Among $NiFe_2O_4$ phases synthesized by sol-gel approaches, the nanostructures sintered at 1000 °C exhibited a capacity retention of about 550 mAh g^{-1} for 50 cycles. According to Lavela et al. , mutually interconnected submicrometer particles with macroporous morphology were required to maintain the high capacity for a greater number of charge/discharge cycles.[17] In our earlier work, we prepared nanophase solid solutions of $(Ni_{1-x}Zn_x)Fe_2O_4$, x = 0 to 1 and investigated the effect of doping $NiFe_2O_4$ by varying Zn composition and subsequent cation redistribution on Li-cycling behavior.[13] The capacity fading between 10 and 50 cycles was lesser than 56 % for x = 0, 0.2, and 0.4 whereas it further decreased to 40% and 18% for x = 0.6 and x = 1. The addition of 20% graphene content to the $NiFe_2O_4$–graphene heterostructures significantly improved the electrochemical performance by effectively preventing the aggregation of nanoparticles during Li-cycling.[18] Recently, Zhao et al. synthesized $NiFe_2O_4$/single-wall carbon nanotube (SWNT) composites with 70 wt % loading ratio using a hydrothermal approach and explored the Li-cycling properties.[19] The composite exhibited a reversible capacity of 776 mAh g^{-1} and maintained it even after 55 cycles during cycling between 0.005 and 3.0 V. The synergistic effect of $NiFe_2O_4$ and SWNT lead to the superior electrochemical performance.

Hence, from the earlier studies, we deduced that, apart from the initial crystal structure and nanosizes, interparticle connectivity of the active material during Li-cycling also plays an important role in affecting the capacity stability of $NiFe_2O_4$.[13,15,16] Interparticle connectivity can be achieved by developing a conducting network throughout the electrode which can be realized by fabricating morphologically stout nanowires/nanofibers of $NiFe_2O_4$ or by the addition of carbon nanofibers or carbon nanotubes along with the active material. Among various synthesis approaches, electrospinning is capable of producing crystalline nanofibers of various electrode materials in pure phase, upon calcining the electrospun precursor/polymer fibers.[20−23] In the present study, continuous nanofibers of $NiFe_2O_4$ are synthesized by the electrospinning approach and subsequent annealing at 500 °C. The electrochemical performance and morphological changes of electrospun $NiFe_2O_4$ nanofibers during the Li-cycling are investigated in detail, and its Li-storage properties are compared with $NiFe_2O_4$ nanoparticles. It is observed that the $NiFe_2O_4$ nanofibers are mechanically robust during charge−discharge cycles and exhibited an excellent electrochemical performance delivering stable high capacity.

EXPERIMENTAL MATERIALS AND METHODS

Polyvinylpyrrolidone (PVP; M_w = 1,300,000) and iron acetylacetonate ($Fe(acac)_3$) and iron nitrate ($Fe(NO_3)$) and nickel acetate dihydrate are purchased from Sigma-Aldrich and Fluka, Singapore. Ethanol (HPLC grade) and glacial acetic acid are purchased from Tedia, Singapore, and used as received.

Electrospinning has been carried out with different precursors and with different concentrations to obtain morphologies like nanofibers and nanoparticles. Firstly, 10 wt % of PVP in 10 mL of ethanol solvent has been prepared and stirred for 1 h at room temperature for complete dissolution. Then, 0.6 g of $Fe(acac)_3$ is added to PVP solution and continuously stirred for a few hours. Later, 1 mL of acetic acid is added, followed by addition of 0.211 g of nickel acetate dihydrate. The solution is stirred again for a few hours. In a similar manner, another precursor solution consisting 1 g of $Fe(NO_3)$ in 10 mL of ethanol solution is prepared and continuously stirred for a few hours. Later, 1 mL of acetic acid is added, followed by addition of 0.3 g of nickel acetate dihydrate. Finally, 10 mL of completely mixed precursor solutions are loaded in a plastic syringe with a hypodermic needle (dia. 22 G). Later, a high-voltage power supply is connected to the needle which is capable of producing direct current voltages of up to 30 kV. Electrospinning is carried out by applying a power supply of around 17.5 kV at the needle with a flow rate ranging from 0.6 to 1 mL/h in a controlled electrospinning setup (Electrospunra, Singapore). Aluminum foil has been used as a counter electrode, and the distance of 15 cm is maintained between the needle and collector. The as-spun green nanofiber mats are vacuum dried at room temperature for overnight to remove the solvent residuals. Then, the electrospun polymeric fibers are calcined at 500 and 800 °C for 5 h in air at a ramping rate of 5 °C/min, and finally, brown $NiFe_2O_4$ samples are obtained and stored carefully.

RESULTS AND DISCUSSION

Figure 1 shows the powder XRD pattern of electrospun polymer precursor fibers calcined at 500 °C, and the formation

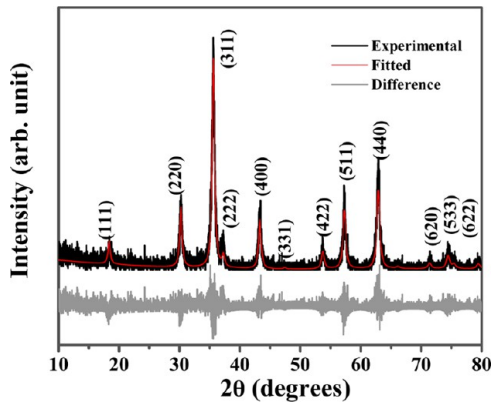

Figure 1. XRD pattern of $NiFe_2O_4$ nanofibers calcined at 500 °C. Miller indices of $NiFe_2O_4$ are shown.

of cubic inverse spinel structure is observed. The lattice parameter value, a (Å) = 8.342, is calculated from the Rietveld refinement which is in good agreement with the reported value (JCPDS No. 74-2081). The XRD pattern of electrospun polymer precursor fibers calcined at 600 and 800 °C are given in the Supporting Information, Figure S1. The crystallite size of $NiFe_2O_4$ fibers calcined at 500, 600, and 800 °C are calculated as 12, 21, and 29 nm using Scherrer's equation, respectively.

Figure 2a shows the SEM images of as-electrospun polymeric precursor fibers before heat treatment. The average diameter of the fibers is ∼250 nm and has a length of several millimeters. The fiber like morphology has been obtained from $Fe(acac)_3$/PVP precursor spun at 17.5 kV with a flow rate of 1 mL/h and sintered at 500 °C (Figure 2b), whereas nanoparticles are obtained upon sintering at 600 and 800 °C (Supporting Information, Figure S2). The TEM images of the nanofibers calcined at 500 °C are shown in Figure 2c,d. After calcination at 500 °C, the fibers remain intact and have an average diameter of 200 nm (Fig. 2d). The scattered dark regions surrounded by bright areas are noticed in Figure 2e, indicating the continuous nanofibers composed of interconnected nanoparticles of size 10−20 nm. The SAED (selected area electron diffraction) pattern shown in Figure 2f consists of diffuse rings clearly indicating the nanophase nature of $NiFe_2O_4$ nanofiber. The d-values calculated from the concentric rings matches well with (220), (311), (400), and (440) $NiFe_2O_4$ planes.

Figure 3a shows the energy dispersive X-ray (EDX) spectrum confirming the presence of Ni, Fe, and O in stoichiometric quantities. The EDX mapping showed the homogeneous

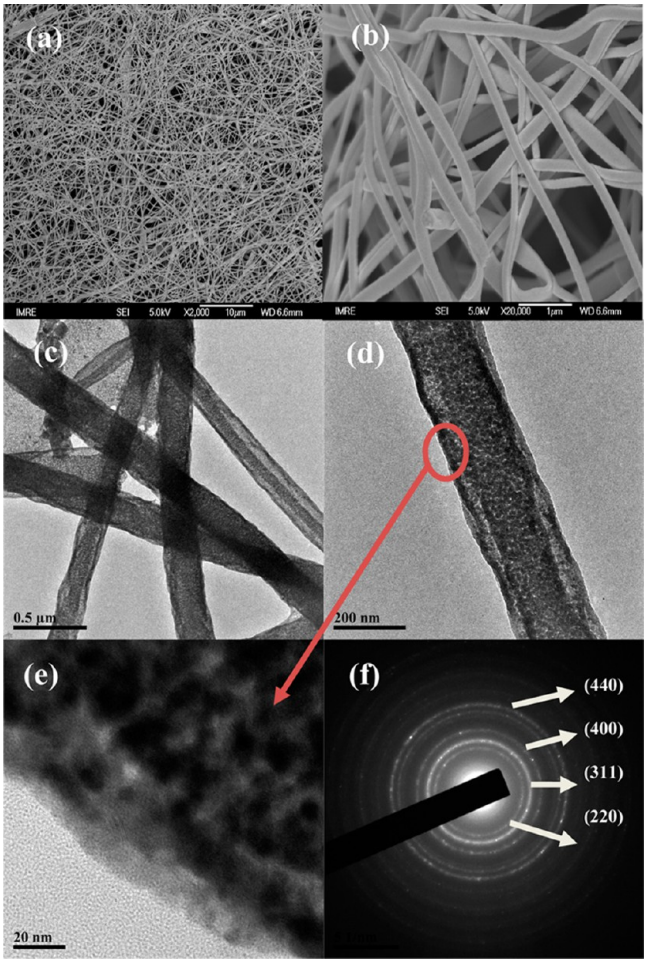

Figure 2. (a) SEM image of electrospun polymer precursor fibers, (b) SEM image of electrospun precursor fibers sintered at 500 °C, (c) TEM image of $NiFe_2O_4$ nanofibers, (d) TEM image of $NiFe_2O_4$ nanofibers, (e) magnified image of an edge of the nanofiber, and (f) SAED pattern of $NiFe_2O_4$ nanofibers. Miller indices are shown.

distribution of three elements in the specific portion (Figure3b) of the $NiFe_2O_4$ nanofiber sample selected for the mapping studies. The nitrogen adsorption and desorption isotherms of $NiFe_2O_4$ nanofibers are shown in the Supporting Information, Figure S3. The BET surface area value is calculated as 50 (±2) m^2/g. $NiFe_2O_4$ nanofibers exhibit a type IV nitrogen isotherm which proceeds via multilayer adsorption followed by capillary condensation. It is a typical adsorption/desorption isotherm of porous solids where capillary condensation and evaporation will not take place at the same pressure, leading to the formation of hysteresis loop in the range of 0.6–1.0 P/P_o.[24]

Li-Cycling Studies. Figure 4 shows the galvanostatic charge–discharge curves of selected cycles of $NiFe_2O_4$ nanofiber composite electrodes, cycled in the range of 0.005–3.0 V at a current rate of 100 mA g^{-1}. 1 Li per formula weight of $NiFe_2O_4$ corresponds to a capacity of 114 mAh g^{-1}. The average charge–discharge potentials are around 1.5 and 1 V, respectively. The first discharge capacity is around 1450 mAh g^{-1} due to an uptake of 12.7 mols of Li. From eq 1, it is obvious that during the first discharge $NiFe_2O_4$ can react only with 8 mols of Li, electrochemically forming Ni and Fe nanoparticles embedded in Li_2O matrix. The observed excess capacity is because of the formation of solid electrolyte interphase (SEI) between the polymeric layer on the metal nanoparticles when

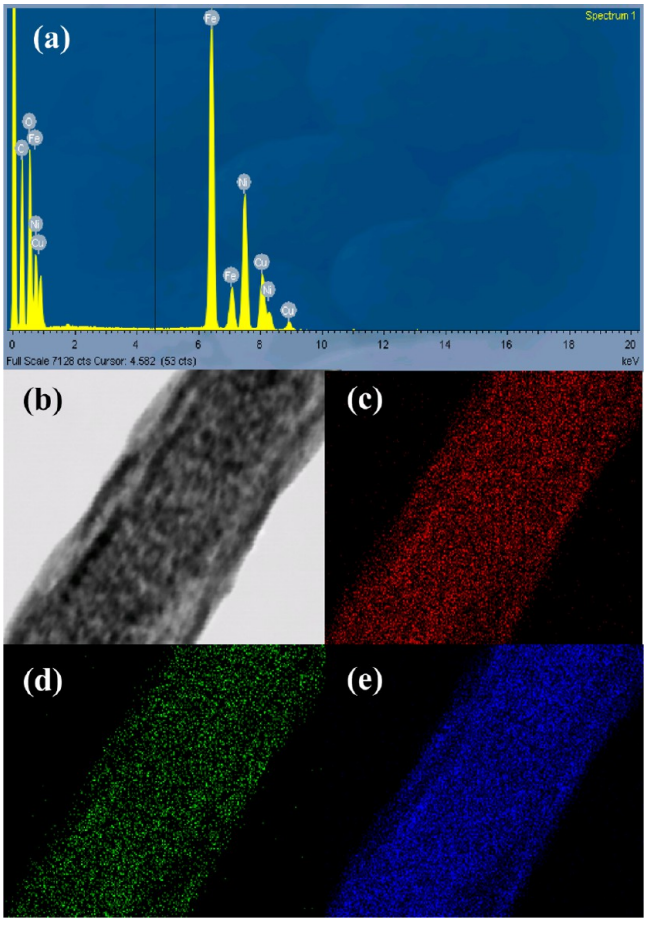

Figure 3. (a) Energy dispersive X-ray (EDX) spectrum of $NiFe_2O_4$ nanofiber sintered at 500 °C, (b) SEM image of the portion selected for EDX analysis, and (c to e) EDX maps of nickel (red), iron (green), and oxygen (blue), respectively.

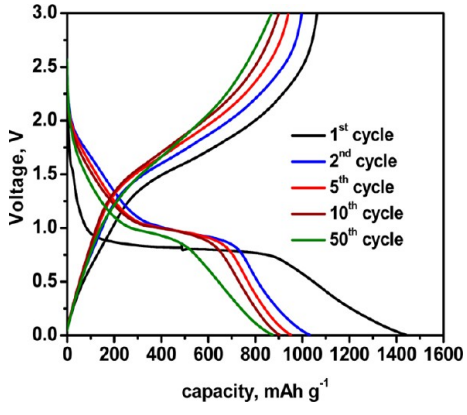

Figure 4. Galvanostatic charge–discharge profiles of $NiFe_2O_4$ nanofibers. Voltage range: 0.005–3 V vs. Li; current: 100 mA g^{-1}.

the electrode potential decreases and approaches to 0.005 V.[12] The nanofibers exhibit first charge capacity of 1000 mAh g^{-1} which is equivalent to 8.8 mols of Li. Theoretical reversible capacity of $NiFe_2O_4$, as indicated in eqs 2 and 3, is 915 mAh g^{-1} which corresponds to reversible uptake and removal of 8 mols of Li.

$$NiFe_2O_4 + 8Li^+ + 8e^- \rightarrow Ni + 2Fe + 4Li_2O \quad (1)$$

dx.doi.org/10.1021/am401779p | ACS Appl. Mater. Interfaces 2013, 5, 9957–9963

$$Ni + Li_2O \leftrightarrow NiO + 2Li^+ + 2e^- \quad (2)$$

$$2Fe + 3Li_2O \leftrightarrow Fe_2O_3 + 6Li^+ + 6e^- \quad (3)$$

Figure 5 illustrates the capacity and coulombic efficiency vs. cycle number plot extracted from galvanostatic cycling data.

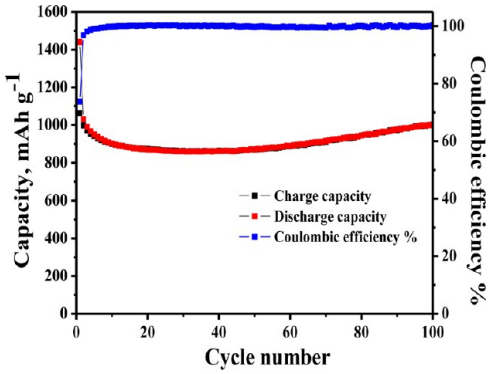

Figure 5. Capacity and coulombic efficiency vs. cycle number plot of $NiFe_2O_4$ nanofibers. Voltage range: 0.005−3 V vs. Li.

Capacity fading is observed during the initial 15 cycles and then stabilized at a capacity of 870 mAh g^{-1} for 40 cycles. Tirado et al. also found similar capacity fading in $NiFe_2O_4$ for the first 20 cycles regardless of the experimental processing conditions.[7,13] After that, the capacity stabilized and continued to fade further depending on the method of synthesis and/or temperature.[18] This initial capacity loss has been considered due to the formation and conditioning of the electrodes during initial cycles.[6,13] Conditioning of the electrodes happen during the initial cycling period where the active materials undergo minor structural rearrangements forming good electrical contacts with the conducting carbons. Thus, the electrochemical grinding effect during cycling leads to disaggregation of the Li_2O/Ni−Fe agglomerations and provokes capacity fading during the initial few cycles.[7]

For electrospun $NiFe_2O_4$ nanofibers, 100% capacity retention is observed between 20 and 40 cycles and then an increase in capacity with 15% rise between 40 and 100 cycles. This increasing tendency of capacity during the galvanostatic cycling is previously observed in other transition metal oxide systems like Fe_3O_4; Zn_2MnO_4, which is due to the reversible growth of a polymeric gel-like film, resulted from kinetically activated electrolyte degradations.[25−27] The charge capacity after the 100th cycle is 1000 mAh g^{-1} which is more or less equal to first charge capacity value. The initial coulombic efficiency is around 80% and increases to 100 % after 8 cycles. The 100% coulombic efficiency is obtained until the 100th cycle due to the stabilization of interface layer (SEI) between the electrode and electrolyte. For comparison, the Li-cycling performances of $NiFe_2O_4$ nanoparticles when cycled in the voltage range of 0.005−3.0 V at a current rate of 100 mA g^{-1} are shown in Figure 6. Nanoparticles are obtained upon sintering electrospun $Fe(NO_3)$ precursor/PVP solution at 600 and 800 °C. It delivers almost similar first discharge capacity as that of the nanofibers. However, the capacity fades rapidly to 345 mAh g^{-1} at the end of 40th cycle. It was reported by Tirado et al.[7] that, among $NiFe_2O_4$ phases prepared by sol-gel approaches by annealing at high temperatures (800−1000 °C), which exhibits better capacity retention, it was around 550 mAh g^{-1} after 50 cycles. In the present case, the precursor

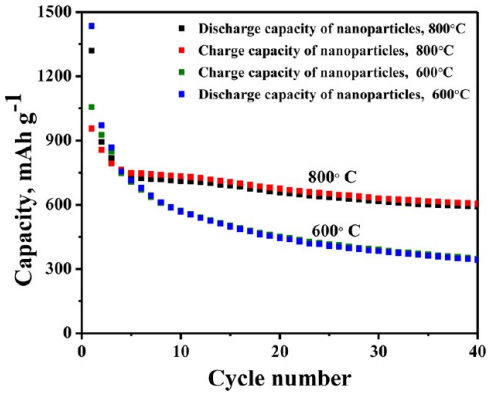

Figure 6. Capacity vs. cycle number plot of $NiFe_2O_4$ nanoparticles. Voltage range: 0.005−3 V vs. Li.

heated to 800 °C, exhibited an enhanced capacity of 600 mAh g^{-1} after 40 cycles in comparison with that calcined at 600 °C. Due to high temperature calcination at 800 °C, nanoparticles tend to get interconnected to form submicrometer particles of $NiFe_2O_4$. As interparticle connectivity is a significant factor in affecting the cycling stability of $NiFe_2O_4$, the 800 °C annealed sample exhibited better cycling performance compared to the 600 °C annealed.[7] However, high temperature sintering increases the crystallinity of the material (Supporting Information, Figure S1), and the degree of crystallinity has an immense influence on the Li-cycling.[28] Hence, proper choice of sintering temperature is a key aspect to obtain better cycling performance.

The cyclic voltammograms (CV) of the $NiFe_2O_4$ nanofibers, up to 6 cycles at the slow scan rate of 58 μVs^{-1} between 0.005 and 3.00 V (vs. Li) are recorded (Supporting Information, Figure S4). Two cathodic peaks located at 0.8 and 1.45 V can be attributed to the reductive reaction of Fe_2O_3 and NiO to Fe and Ni metal, respectively. A broad anodic peak at ∼1.6 V is observed with a slight shift in the charge cycle, and the broad peak may include the peaks related to oxidation of Fe and Ni nanoparticles as per eqs 2 and 3. According to the earlier reports, the oxidation of Fe^0 and Ni^0 to Fe^{3+} and Ni^{2+} occurs at ∼1.7 V, and it agreed well with our observation.[29]

The superior electrochemical performance of the $NiFe_2O_4$ nanofibers can be due to its porous nature and higher surface area which provides easy accessibility of electrolyte and empty spaces to accommodate volume change during conversion reactions.[30,31] The effect of morphology on cycling performance is investigated by using microstructural images of $NiFe_2O_4$ nanofibers obtained before and after Li-cycling. Figure 7a,b shows the SEM images of $NiFe_2O_4$ nanofiber−composite electrode before Li-cycling whereas Figure 7c,d displays SEM images of the cycled electrode after 50 charge−discharge cycles. As can be clearly seen, bare composite electrode consists of smooth interconnected fibers, surrounded by conducting carbon additives. The small lumps of particles observed in Figure 7a,b are Super P carbon added during electrode fabrication. It is obvious from the Figure 7c,d that the nanofibers remain unbroken upon Li-cycling but the surface smoothness of the fibers is lost due to the electrochemical reactions. The absence of capacity fading can be attributed to the unique morphology of the electrospun fibers which remains intact throughout the cycling. It should be noted that the particle lumps of conducting carbon can no longer be seen in cycled electrode. The inset of Figure 7d shows the closer image

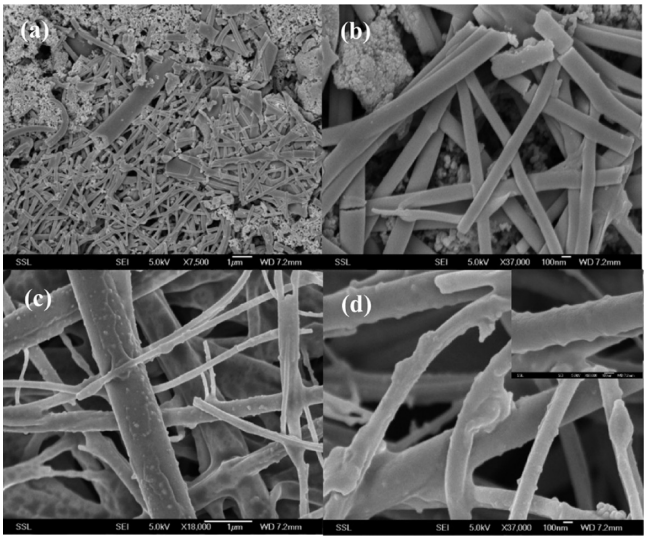

Figure 7. SEM image of $NiFe_2O_4$ nanofiber electrode before cycling at (a) lower magnification and (b) higher magnification; SEM image of cycled $NiFe_2O_4$ nanofiber electrode (after 50 charge−discharge cycles) at (c) lower magnification and (d) higher magnification (inset shows the cycled single nanofiber in expanded scale).

of cycled nanofibers, and the observed "bumpy" surface morphology is due to the presence of carbon additives which got embedded within the surface layer formed during electrode−electrolyte interaction.

Figure 8 shows the high resolution TEM images of $NiFe_2O_4$ fiber composite electrodes after 100 charge−discharge cycles.

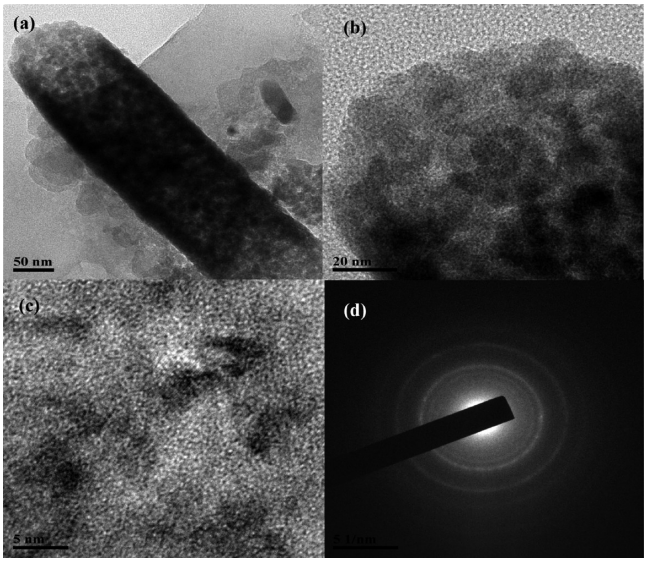

Figure 8. (a) TEM image of particles of cycled electrodes of $NiFe_2O_4$ nanofibers (100^{th} cycle; charged to 3 V). (b) Magnified TEM image of an edge of the selected nanofiber. (c) HRTEM image of $NiFe_2O_4$ nanofibers composite electrode after cycling. (d) SAED pattern of $NiFe_2O_4$ nanofibers composite electrode after cycling.

Interestingly, fiber like morphology is preserved even after 100 cycles which is well evident from the TEM image (Figure 8a). Figure 8b shows the magnified image of the edge of the selected cycled nanofiber (after 100 cycles) with dark and light areas depending on the degree of crystallinity of the $NiFe_2O_4$. Ex situ SAED studies are carried out on the $NiFe_2O_4$ nanofiber charged electrodes to identify the crystallinity of the oxide phases formed during Li-cycling. The HRTEM lattice image (Figure 8c) clearly shows the nanocrystalline regions of size ∼5 nm dispersed in an amorphous medium which can be considered as the presence of Fe_2O_3 and NiO nanoparticles in an amorphous Li_2O matrix. The SAED pattern (Figure 8d) displays only diffuse rings which indicate the presence of the predominant amorphous nature of the active material after 100 charge−discharge cycles.

Electrochemical Impedance Studies. Electrochemical impedance studies (EIS) provide detailed information on charge transfer, surface film, bulk resistance and capacitance of the electrodes, and its variations with the applied voltage when charging and discharging.[32] EIS are carried out on $NiFe_2O_4$ nanofibers at selected voltages ranging from 0.005 to 3.0 V vs. Li at room temperature. The cells are charged or discharged to the selected voltages and relaxed for 3 h, and the impedance spectra are measured. The impedance data are analyzed by fitting an equivalent electrical circuit as shown in Figure 9a; the circuit is similar to that reported in the literature.[32] R_1 denotes electrolyte resistance; R_{sf} and C_{sf} are resistance and capacitance of the interface layers formed on the electrode surfaces. R_{dl} and C_{dl} are faradic charge transfer resistance and relative double-layer capacitance. The contribution to R_b is due to the bulk resistance of the cell.[33,34]

W is the Warburg impedance related to the combination of diffusional effects of lithium-ion at the interface between the electrolytes and active material particles. The combination of R_{ct} and W is called faradic impedance, reflecting the kinetic of cell reactions. Lower R_{ct} corresponds to a faster kinetic of the faradic reactions. Figure 9b shows the Nyquist plots (Z' vs. $-Z''$) of the fresh cell at open circuit voltage (OCV), fresh cell discharge to 1 V, and cell discharged to 0.005 V after the 1^{st} and 10^{th} discharge step. A semicircle is observed in the high-to-medium frequency range indicating that effects of the surface film and the charge transfer are not separable. In this case, the curve fitting is carried out using R_{sf+ct} combinations since both electronic and ionic charge transfers are involved in the discharge process. The fresh cell (OCV ∼ 2.8 V) shows a broad depressed semicircle in the high/intermediate frequency region (> 20 Hz), which is after curve fitting revealed an impedance of 250 (± 3) Ω attributed mainly to R_{sf}. The R_{sf} value is the measure of the hindrance for Li-ion conduction through the SEI layer. The associated capacitance (C_{sf}) is 20 (± 5) μF. According to Chamas et al.,[35] in the pristine state, the impedance spectra evolves by a high-frequency semicircle associated with native SEI films at the electrodes, followed by a low-frequency line related to the mass transports and cell capacitances. The spectrum measured after discharge to 1 and 0.005 V differs significantly from that initially recorded at the OCV (Figure 9b). The spectrum at the end of first discharge to 1 V shows a high frequency depressed semicircle with reduced diameter followed by a well-defined Warburg region (α = 40−45°) and an intercalation capacitance region (α' = 60−65°) at low frequencies. This shows that the contribution is from R_{sf+ct} only, and the bulk resistance (R_b) is negligibly small. At 0.005 V, apart from the high frequency semicircle, the spectrum shows an undeveloped semicircle before the Warburg region which is almost a straight line parallel to the x-axis. This observation is due to the contribution from the bulk resistance of composite electrode (R_b) to the overall impedance. The observation may be due to the crystal structure destruction happening below 1 V. Accordingly, the R_b and CPE_b

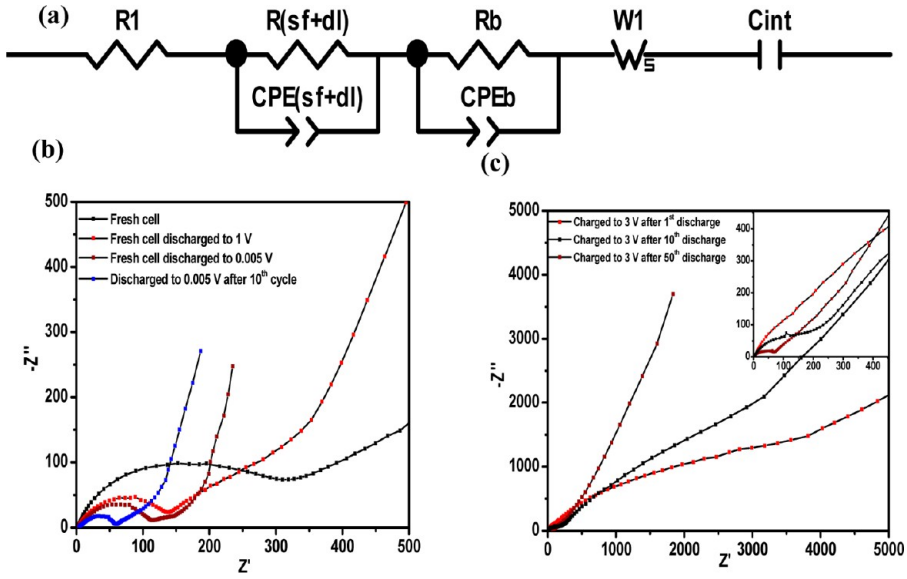

Figure 9. (a) Equivalent electrical circuit model consisting of resistances (R_i), constant phase elements (CPEs), Warburg impedance (Ws), and intercalation capacitance (C_{int}). (b) Nyquist plots (Z' vs. $-Z''$) of $NiFe_2O_4$ nanofibers at open circuit voltage and discharged state (0.005 V vs. Li) at various discharge−charge cycles. (c) Nyquist plots (Z' vs. $-Z''$) of $NiFe_2O_4$ nanofibers in the charged state (0.005 V vs. Li) at various discharge−charge cycles. Inset shows the low high frequency region in the expanded scale.

components in the circuit (Figure 9a) are used to fit the spectrum. Interestingly, at the end of deep discharge after 10 cycles, the R_{sf+ct} value decreases considerably to 55 Ω. Thus, from Figure 9b, it can be concluded that, during initial cycles, R_{sf+ct} values are high due to the initiation of the displacement redox reaction of Li with $NiFe_2O_4$ nanofibers. The gradual drop in R_{sf} values is indicative of the stabilization of SEI layers and supporting the stable capacity behavior of $NiFe_2O_4$ nanofibers after a few initial cycles. R_{ct} and R_b values increase during initial cycles which are in good agreement with capacity fading behavior noticed in the initial 10 cycles.

During the initial cycles, the material undergoes a large unit cell volume change due to the electrochemical conversion reaction, with cracking of the electrode and subsequent reduction in electronic conductive path. There will also be an increase in internal defects and isolated active regions unreacted with electrolytes which can lead to an increase in the charge transfer resistance. By the end of 10th cycle, conditioning of the electrode will be completed and there will be better contact between active materials and electrolyte; therefore, R_{sf+ct} will be stabilized thereafter. Impedance spectra of the cell charged to 3 V after the 1st, 10th, and 50th discharge steps are shown in Figure 9c. For the cell charged to 3 V after the 1st discharge, a large depressed semicircle which spans from 1 MHz to 0.1 Hz can be clearly seen. It is followed by a Warburg region at frequencies less than 0.1 Hz. The calculated resistance value is in the order of 3 KΩ. For the cell charged to 3 V after the 10th discharge, two depressed semicircles appear, one with shorter diameter at high frequencies and the other with longer diameter occurring at intermediate frequency. Equivalent circuit fitting of the spectra indicates a decrease in R_{sf+ct} (133 Ω) and increase in R_b during the 10th charge. For the 50th cycle, the resistance R_{sf+ct} value significantly reduces to 50 Ω which is well evident from the small semicircle found in high frequency region >40 Hz with a negligible charge transfer resistance (inset of Figure 9c). The R_{sf+ct} value is almost similar to that in the fully discharged state after the 10th cycle. This behavior corroborates very well with the stable capacity behavior shown by the $NiFe_2O_4$ nanofiber electrodes, between 10 and 50 cycles.

CONCLUSION

Continuous $NiFe_2O_4$ nanofibers have been prepared by electrospinning of $Fe(acac)_3$/PVP-based precursors and subsequent annealing at 500 °C. The nanofibers exhibited a high discharge capacity of 870 mAh g^{-1} with superior cycling stability than that of nanoparticles. An increase in capacity is observed after 40 cycles, and a reversible capacity of 1000 mAh g^{-1} is obtained at the end of 100 cycles. The fiber like morphology remains intact even after 100 charge/discharge cycles. The morphological robustness of nanofibers during conversion reaction is a unique feature that enables one to maintain a conductive network throughout the electrode. The excellent Li-storage properties indicate that the porous $NiFe_2O_4$ nanofibers can find promising applications in high capacity Li-ion batteries.

ASSOCIATED CONTENT

Supporting Information

The characterization details and the procedure for fabrication of coin test cells. XRD pattern and nitrogen adsorption−desorption isotherm of $NiFe_2O_4$ nanoparticles, SEM images of $NiFe_2O_4$ nanoparticles synthesized by different routes, and cyclic voltammogram of $NiFe_2O_4$ nanofibers. This material is available free of charge via the Internet at http://pubs.acs.org.

AUTHOR INFORMATION

Corresponding Authors

*E-mail: seeram@nus.edu.sg.
*E-mail: phychowd@nus.edu.sg.

Author Contributions

‡C.T.C. and J.S. contributed equally.

Notes

The authors declare no competing financial interest.

REFERENCES

(1) Cao, G.; Wang, Y. *Nanostructures and Nanomaterials: Synthesis, Properties, and Applications*; World Scientific: Singapore, 2011; Vol. 2, p 581.
(2) Nazri, G.-A.; Pistoia, G. *Lithium Batteries: Science and Technology*; Springer: New York, 2003; p 728.
(3) Daiwon, C.; Wei, W.; Zhenguo, Y. Material Challenges and Perspectives. In *Lithium-Ion Batteries*; CRC Press: Boca Raton, FL, 2011; pp 1−50.
(4) Poizot, P.; Laruelle, S.; Grugeon, S.; Dupont, L.; Tarascon, J. M. *Nature* **2000**, *407*, 496−499.
(5) Taberna, P. L.; Mitra, S.; Poizot, P.; Simon, P.; Tarascon, J. M. *Nat. Mater.* **2006**, *5*, 567−573.
(6) Sharma, Y.; Sharma, N.; Subba Rao, G. V.; Chowdari, B. V. R. *Electrochim. Acta* **2008**, *53*, 2380−2385.
(7) Vidal-Abarca, C.; Lavela, P.; Tirado, J. L. *J. Phys. Chem. C* **2010**, *114*, 12828−12832.
(8) Sivakumar, N.; Gnanakan, S. R. P.; Karthikeyan, K.; Amaresh, S.; Yoon, W. S.; Park, G. J.; Lee, Y. S. *J. Alloys Compd.* **2011**, *509*, 7038−7041.
(9) Bonino, C. A.; Ji, L.; Lin, Z.; Toprakci, O.; Zhang, X.; Khan, S. A. *ACS Appl. Mater. Interfaces* **2011**, *3*, 2534−2542.
(10) Sharma, Y.; Sharma, N.; Subba Rao, G. V.; Chowdari, B. V. R. *Bull. Mater. Sci.* **2009**, *32*, 295−304.
(11) Reddy, M. V.; Subba Rao, G. V.; Chowdari, B. V. R. *Chem. Rev.* **2013**, *113*, 5364−5457.
(12) Chen, C. J.; Greenblatt, M.; Waszczak, J. V. *Solid State Ionics* **1986**, *18−19* (Part 2), 838−846.
(13) Cherian, C.; Reddy, M. V.; Subba Rao, G. V.; Sow, C.; Chowdari, B. V. R. *J. Solid State Electrochem.* **2012**, *16*, 1823−1832.
(14) Hailiang, W.; Yongye, L.; Ming, G.; Yanguang, L.; Wesley, C.; Tyler, M.; Jigang, Z.; Jian, W.; Tom, R.; Fei, W.; Hongjie, D. *Nat. Commun.* **2012**, *3*, 917−917.
(15) Lavela, P.; Tirado, J. L. *J. Power Sources* **2007**, *172*, 379−387.
(16) Alcántara, R.; Jaraba, M.; Lavela, P.; Tirado, J. L.; Jumas, J. C.; Olivier-Fourcade, J. *Electrochem. Commun.* **2003**, *5*, 16−21.
(17) Lavela, P.; Kyerematenga, N. A.; Tirado, J. L. *Mater. Chem. Phys.* **2010**, *124*, 102−108.
(18) Fu, Y.; Wan, Y.; Xia, H.; Wang, X. *J. Power Sources* **2012**, *213*, 338−342.
(19) Zhao, Y.; Li, J.; Ding, Y.; Guan, L. *J. Mater. Chem.* **2011**, *21*, 19101−19105.
(20) Ramakrishna, S.; Fujihara, K.; Teo, W.-E.; Yong, T.; Ma, Z.; Ramaseshan, R. *Mater. Today* **2006**, *9*, 40−50.
(21) Teh, P. F.; Pramana, S. S.; Sharma, Y.; Ko, Y. W.; Madhavi, S. *ACS Appl. Mater. Interfaces* **2013**, *5*, 5461−5467.
(22) Xue, L.; Fu, K.; Li, Y.; Xu, G.; Lu, Y.; Zhang, S.; Toprakci, O.; Zhang, X. *Nano Energy* **2013**, *2*, 361−367.
(23) Cheah, Y. L.; Aravindan, V.; Madhavi, S. *ACS Appl. Mater. Interfaces* **2013**, *5*, 3475−3480.
(24) Agarwala, S.; Lim, Z. H.; Nicholson, E.; Ho, G. W. *Nanoscale* **2012**, *4*, 194−205.
(25) Zhang, G.; Yu, L.; Wu, H. B.; Hoster, H. E.; Lou, X. W. *Adv. Mater.* **2012**, *24*, 4609−4613.
(26) Zhou, G.; Wang, D.-W.; Li, F.; Zhang, L.; Li, N.; Wu, Z.-S.; Wen, L.; Lu, G. Q.; Cheng, H.-M. *Chem. Mater.* **2010**, *22*, 5306−5313.
(27) Grugeon, S.; Laruelle, S.; Dupont, L.; Tarascon, J. M. *Solid State Sci.* **2003**, *5*, 895−904.
(28) Cherian, C. T.; Reddy, M. V.; Haur, S. C.; Chowdari, B. V. R. *RSC Advances* **2013**, *3*, 3118−3123.
(29) Zhao, H.; Zheng, Z.; Wong, K. W.; Wang, S.; Huang, B.; Li, D. *Electrochem. Commun.* **2007**, *9*, 2606−2610.
(30) Cho, J. *J. Mater. Chem.* **2010**, *20*, 4009−4014.
(31) Ge, M.; Rong, J.; Fang, X.; Zhou, C. *Nano Lett.* **2012**, *12*, 2318−2323.
(32) Das, B.; Reddy, M. V.; Krishnamoorthi, C.; Tripathy, S.; Mahendiran, R.; Subba Rao, G. V.; Chowdari, B. V. R. *Electrochim. Acta* **2009**, *54*, 3360−3373.
(33) Huang, J. S.; Yang, L.; Liu, K. Y.; Tang, Y. F. *J. Power Sources* **2010**, *195*, 5013−5018.
(34) Levi, M. D.; Aurbach, D. *J. Phys. Chem. B* **2004**, *108*, 11693−11703.
(35) Chamas, M.; Lippens, P. E.; Jumas, J. C.; Hassoun, J.; Panero, S.; Scrosati, B. *Electrochim. Acta* **2011**, *56*, 6732−6736.